

Invertible optical nonlinearity in epsilon-near-zero materials

Chentao Li ,¹ Xinyu Tian,¹ Guoce Yang ,¹ Sukrith U. Dev,² Monica S. Allen,² Jeffery W. Allen,² and Hayk Harutyunyan^{1,*}

¹Department of Physics, Emory University, 400 Dowman Drive, Atlanta, Georgia 30324, USA

²Air Force Research Laboratory, Munitions Directorate, Eglin AFB, Florida 32542, USA



(Received 30 March 2022; accepted 8 February 2023; published 22 March 2023)

Epsilon-near-zero (ENZ) materials such as indium tin oxide (ITO) have recently emerged as a new platform to enhance optical nonlinearities. Here we report a theoretical and experimental study on the origin of nonlinearities in ITO films that are dominated by intraband and interband transitions. We show that there are two competing factors that jointly contribute to a spectrally invertible nonlinearity of ITO near its ENZ region, i.e., the nonparabolicity of the bands that results in a larger effective mass, and the Fermi energy shift that determines the free carrier density. Our work reveals the relationship between the large nonlinearity and the intrinsic material properties of the ITO films, which will enable design and development of photonic materials and nonlinear devices made of transparent conductive oxides.

DOI: [10.1103/PhysRevResearch.5.013198](https://doi.org/10.1103/PhysRevResearch.5.013198)

I. INTRODUCTION

The pursuit of a large nonlinearity with a moderate excitation field has been a long-time goal in optics. To that end, most approaches have been focused on materials whose refractive index (RI) can be drastically modified using an optical pump [1,2]. Recently, epsilon-near-zero (ENZ) materials have emerged as intriguing platforms exhibiting diverging velocities [3,4], wavelength expansion [5], and large field enhancement [6–8]. In addition to the linear effects in ENZ [9,10], studies have revealed the potential of ENZ materials in nonlinear applications [11]. Intuitively, the change of RI can be expressed as $dn = d\epsilon/2\sqrt{\epsilon}$, which becomes significant given a near-zero permittivity $\epsilon \approx 0$.

Transparent conductive oxides (TCOs) are often used as strongly nonlinear ENZ platforms [12–15]. Typical examples include Al- or Ga-doped zinc oxides (AZO/GZO) [12,16,17], cadmium oxides (CdO) [18,19], and indium tin oxide (ITO) [20,21]. These materials support ENZ resonances in the near-infrared (NIR) range and are compatible with existing complementary metal oxide semiconductor (CMOS) technologies [22,23], thus showing great promise for applications in telecom industries [24]. Moreover, the stability of these materials is better than traditional metals [25] and highly doped semiconductors [26] that show near-zero ϵ at their bulk plasma wavelengths. This rich design space for photon manipulation enables different strategies to enhance the nonlinearity, including patterned structures [27,28], plasmonic materials [20,29–31], and waveguide modes [32].

In recent studies strong optical nonlinearities, including RI change dn on the order of unity, were observed in ITO

thin films [6,8,15,16,20,33,34]. The transient response is dominated by two subpicosecond (ps) processes: (i) intraband transition excited by pump photons with sub-band-gap energies; and (ii) interband transition, pumped with high-energy UV photons. Understanding the origin of the nonlinearity observed in ultrafast experiments necessitates effective modeling of these two processes [6,20,21,35]. Interband transition is described by carrier generation followed by trap-assisted recombination [8]. For intraband transitions, an optical Kerr effect model was proposed where the plasma frequency ω_p or the RI n is linearly dependent on the pump intensity, enabling quantitative description of the nonlinearity [15,36]. Specifically, using the electron-phonon coupling as a fitting parameter, the two-temperature model revealed that the rise of the electron temperature due to laser excitation generates a temperature-dependent complex index [6,8,20]. Alternatively, a deterministic physical model attributed the nonlinearity to a nonparabolic conduction band, which modifies the effective mass for the excited hot electron population [19,28,37,38]. However, to our knowledge, no unified description exists for the excited-state dynamics and instead, these mechanisms are modeled as separate processes when explaining the origin of the nonlinearity, while their joint contributions and simultaneous interactions remain unexplored. Specifically, the influence of the nonparabolicity on the interband transition has never been investigated.

Here we adopt a conceptually different approach by exploring optical nonlinearities in ENZ materials under various interaction regimes and material parameters, discovering a different type of spectrally invertible nonlinear response in ITO films. Our theory predicts that by varying the nonparabolicity and the Fermi level of ITO, the ENZ resonance shift can be tuned to occur in opposite spectral directions, giving rise to transient transmittance signals with highly variable spectral shapes. This prediction is confirmed using femtosecond (fs) pump-probe measurements with broadband probe beams on ITO films with different ENZ wavelengths. The nonparabolicity of the bands and the free carrier density are shown to be

*hayk.harutyunyan@emory.edu

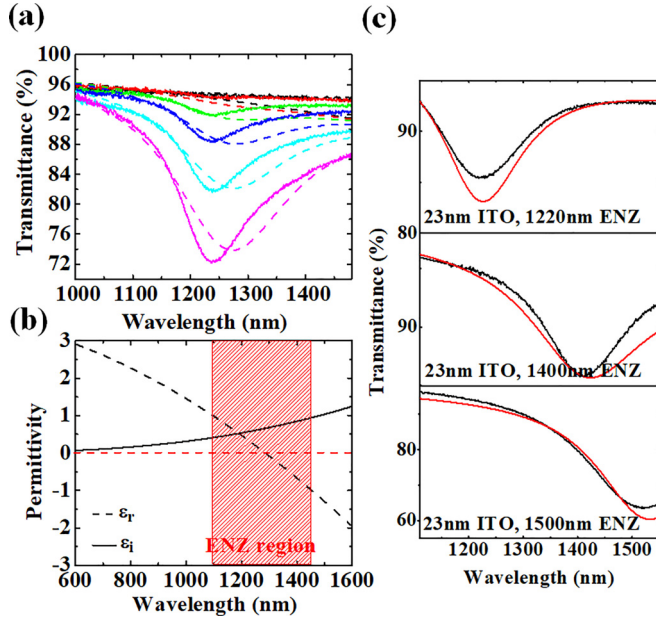


FIG. 1. (a) Transmittance of the commercial ITO film at different incident angles: 15° (black), 30° (red), 45° (blue), 60° (azure), and 75° (magenta). Solid curves are experimental data and dashed curves are calculated using TMM. (b) Calculated permittivity using the fitted Drude parameters. (c) Experimental (black line) and calculated (red line) 60° transmittance spectra of sputtered ITO films with different ENZ wavelengths.

two competing factors that jointly contribute to the invertible nonlinearity, revealing the relationship between the large optical nonlinearity and the intrinsic dispersion relations of ITO films in the ENZ region.

II. LINEAR OPTICAL PROPERTIES

Figure 1(a) shows the linear optical properties of a 23-nm-thick commercial ITO film on a glass substrate. The oblique-angle transmittance reveals a resonant ENZ peak at 1240 nm, with its amplitude increasing at larger incident angles. From boundary conditions we have $\epsilon_0 E_{0\perp} = \epsilon_1 E_{1\perp}$, where ϵ_0 and ϵ_1 are permittivity of air and the ITO film, respectively, and $E_{0\perp}$ and $E_{1\perp}$ are the normal components of the electric field. Thus, for a small ϵ_1 in the ENZ region, the field normal to the ITO film would be enhanced with larger incident angles producing stronger field enhancement. A Drude model can be used to describe the permittivity of ITO films near the ENZ region:

$$\epsilon(\omega) = \epsilon_\infty - \frac{\omega_p^2}{\omega^2 + i\gamma_p\omega}. \quad (1)$$

The transfer matrix method (TMM) [39] is used to calculate the reflectance and transmittance of the ITO thin films after obtaining the thickness and the permittivity. Combining the Drude model and TMM, the linear transmittance spectra of ITO films are fitted to extract parameters ω_p and γ_p . Here ω_p represents the plasma frequency without a pump $\omega_{p,umpump}$. Figure 1(a) shows the calculation result using $\omega_p = 1.9$ and $\gamma_p = 0.17$ eV, which show good agreement with the experiments. The calculated dispersion of ITO with these Drude

parameters is shown in Fig. 1(b). The real part of the permittivity switches sign at 1240 nm and defines the ENZ region with $\epsilon_r < 1$ [shaded area in Fig. 1(b)]. More ITO films with the same thickness, 23 nm, are fabricated with rf magnetron sputtering on glass substrates, followed by different annealing processes to obtain different ENZ wavelengths. (See Appendix A for fabrication details and Fig. 2 for atomic force microscopy images of ITO films [40]). The measured and fitted transmittance spectra of three samples at 60° excitation angle are shown in Fig. 1(c) featuring different ENZ resonances.

III. THEORETICAL MODEL OF INVERTIBLE OPTICAL NONLINEARITY

Figure 3 shows the schematic of the transient processes. When the NIR pump photon energy is smaller than the band gap, the electrons in the conduction band undergo an intraband transition through free carrier absorption. Before absorption, the electron equilibrium can be described as a room-temperature Fermi distribution. Once the pump photon is absorbed and hot electron distribution is formed, the effective mass of the electron sea is increased due to the nonparabolicity of the conduction band. This redshifts the ENZ resonance by decreasing the plasma frequency ω_p ,

$$\omega_p = \sqrt{\frac{ne^2}{\epsilon_0 m^*}}, \quad (2)$$

where n is the free electron density and m^* is the effective mass of the conduction band. Conversely, when the photon energy is greater than the band gap (UV photons), an interband transition occurs and the free carrier concentration n is increased, which increases ω_p [Eq. (2)], blueshifting the ENZ resonance. However, the increased free carrier density raises the Fermi level, which also increases m^* due to the nonparabolicity. Thus, when the nonparabolicity of the material is large enough, m^* increase dominates the free carrier density increase, and interband transition can cause an overall redshift of ENZ, inverting the nonlinearity. The total change and the shift direction of ω_p and the nonlinearity will depend on the competing contributions of the free carrier density at the equilibrium and the nonparabolicity of the conduction band.

To evaluate the influence of both factors on the nonlinearity of ITO, an analytical model is developed. First, to account for nonparabolicity, the band structure $E(k)$ is written as [41,42]

$$\frac{k^2 \hbar^2}{2m^*} = E(k) + \frac{E^2}{E_g}, \quad (3)$$

where $1/E_g$ denotes the nonparabolicity. From the collisionless Boltzmann equation, the plasma frequency ω_p is derived as [28]

$$\omega_{p,pump}(\mu, T)^2 = \frac{e^2}{3m^*\pi^2} \int_0^\infty \left[\frac{2m^*}{\hbar^2} \left(E + \frac{E^2}{E_g} \right) \right]^{\frac{3}{2}} \times \left(1 + \frac{2E}{E_g} \right)^{-1} \left(-\frac{\partial f_0(\mu, T)}{\partial E} \right) dE, \quad (4)$$

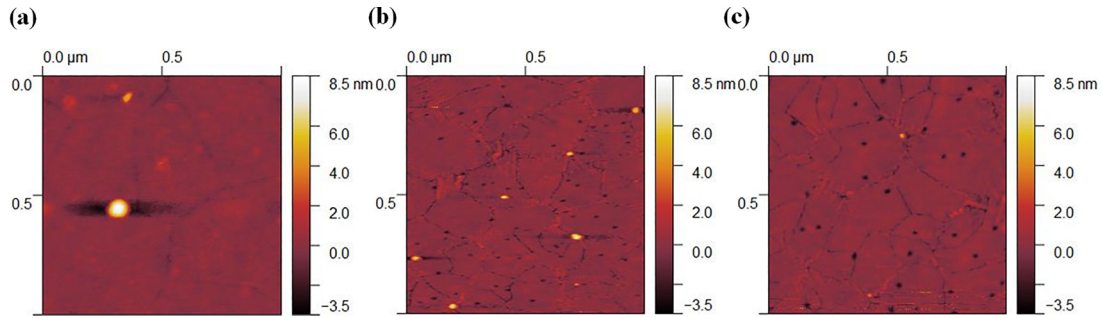


FIG. 2. Atomic force microscopy scan images of homemade ITO films with the ENZ wavelengths at (a) 1220 nm, (b) 1400 nm, and (c) 1500 nm. The surface roughness is (a) 0.59 nm, (b) 0.52 nm, and (c) 0.43 nm, respectively.

where $f_0(\mu, T)$ represents the Fermi-Dirac distribution, μ is the chemical potential, and T is the electron temperature. Meanwhile the electron density is

$$n(\mu, T) = \frac{1}{\pi^2} \int_0^\infty \left[\frac{2m^*}{\hbar^2} \left(E + \frac{E^2}{E_g} \right) \right]^{\frac{1}{2}} \times \frac{m^*}{\hbar^2} \left(1 + \frac{2E}{E_g} \right) f_0(\mu, T) dE. \quad (5)$$

The energy density is given by

$$U(\mu, 300K) + dU = \frac{1}{\pi^2} \int_0^\infty \left[\frac{2m^*}{\hbar^2} \left(E + \frac{E^2}{E_g} \right) \right]^{\frac{1}{2}} \times E \frac{m^*}{\hbar^2} \left(1 + \frac{2E}{E_g} \right) f_0(\mu, T) dE, \quad (6)$$

where dU is the absorbed energy density after pump. For the intraband transition, the free carrier density $n(\mu, T)$ is a constant and the electron energy density $U(\mu, T)$ is equal to the room-temperature energy density $U(\mu, 300\text{ K})$ plus the absorbed pump photon energy density dU . Therefore the intraband nonlinearity is fully determined by the parameters m^* , E_g , ω_p , and γ_p . In Figs. 4(a) and 4(b), we explore the differential transmittance change ΔA near the ENZ region under the NIR pump, where intraband transition dominates the nonlin-

earity. ΔA is defined as $-\log(1 + \Delta T/T_0)$, where T_0 denotes the reference transmittance and ΔT is the dynamic change in transmittance after the pump. In Fig. 4(a) the ENZ wavelength is varied from 1220 to 1500 nm while the nonparabolicity E_g and m^* are kept at 2.39 eV and $0.26m_0$, respectively, where m_0 is the electron mass at rest. At longer ENZ wavelengths that correspond to the lower free carrier density and lower Fermi level, the maximum absolute value of ΔA is larger. This is because electrons at a lower Fermi level undergo a larger change in effective mass when the same amount of energy is absorbed, which results in a larger nonlinearity. Conversely, as shown in Fig. 4(b), when the ENZ wavelength is kept unchanged, increasing E_g from 2 to 3.3 eV results in decreasing ΔA values. Smaller E_g represents larger nonparabolicity, thus creating a larger change in m^* and a larger nonlinearity.

After considering the nonlinearity under the NIR pump dominated only by intraband transitions, we introduce a phenomenon which involves both intraband and interband transitions under a UV pump. Here, the free carrier density $n(\mu, T)$ is equal to the room-temperature carrier concentration $n(\mu, 300\text{ K})$ plus the density of absorbed photons dn :

$$n(\mu, 300K) + dn = \frac{1}{\pi^2} \times \int_0^\infty dE \left[\frac{2m}{\hbar^2} \left(E + \frac{E^2}{E_g} \right) \right]^{\frac{1}{2}} \frac{m}{\hbar^2} \times \left(1 + \frac{2E}{E_g} \right) f_0(\mu, T), \quad (7)$$

where dn is given by

$$dn = \frac{F A \cos\theta}{\pi r^2 h E_{\text{photon}}}, \quad (8)$$

where F is the energy per pulse, A is the absorption, θ is the incident angle, r is the pump beam radius, h is the film thickness, and E_{photon} is the photon energy. The calculated ΔA is plotted in Fig. 4(c), where the ENZ wavelength is 1220 nm and E_g is varied from 2 eV to 3.3 eV. Interestingly, unlike in Figs. 4(a) and 4(b), where the NIR pump causes an unchanged spectral shape of ΔA regardless of the values of E_g and ENZ, the spectral shape under the UV excitation in Fig. 4(c) depends on the relative strength between the free carrier density and the nonparabolicity. For small E_g [Fig. 4(c), black curve], the hot-electron-induced Fermi-level shift has a stronger contribution than the increase in carrier density due to band-to-band transition and causes a redshift of ω_p . Conversely, an overall blueshift of ω_p occurs when the hot

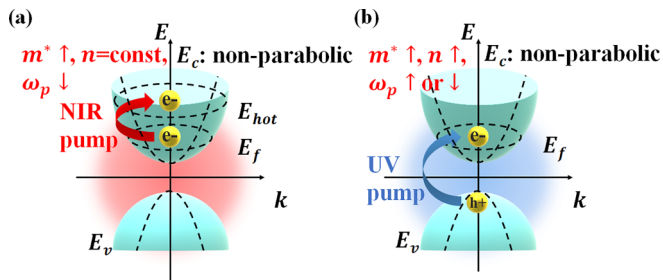


FIG. 3. Schematic of the nonlinear optical responses in ITO films. The intraband transition under the NIR pump induces a larger effective mass due to the nonparabolic band structure and decreases the plasma frequency. The interband transition under the UV pump generates additional free carriers, increases the plasma frequency, and induces a larger effective mass. E_c : conduction band, E_f : Fermi level, E_v : valence band, E_{hot} : hot electron energy level, and dashed curves represent the parabolic bands and the increase of the Fermi level.

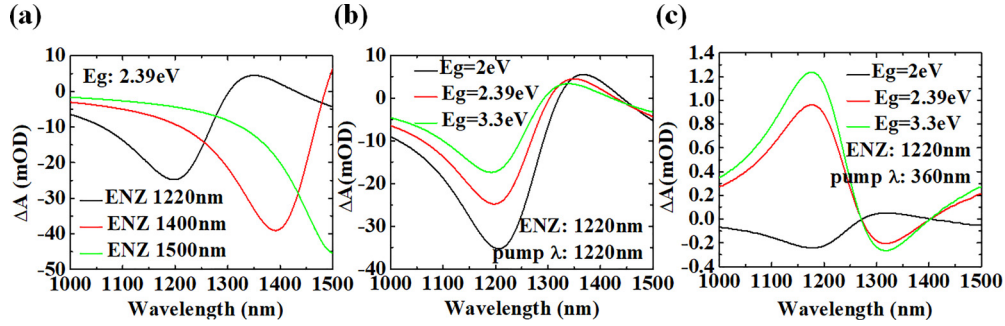


FIG. 4. (a) Differential transmittance change ΔA under NIR excitation for $E_g = 2.39$ eV. (b) Calculated ΔA for different values of E_g under NIR excitation. (c) Calculated ΔA for different values of E_g under UV excitation.

electron contribution is relatively lower [Fig. 4(c), red and green curves]. We observed spectral inversion of nonlinearity based on the competing mechanisms of the free carrier density changes and the nonparabolicity.

IV. ULTRAFAST EXPERIMENTAL RESULTS

To verify these predictions, we carry out a set of transient transmittance measurements using a narrow-band

femtosecond pump and broadband femtosecond probe pulses (see Appendix A for experimental details). Figure 5(a) shows the ΔA spectral map measured on an ITO film with both the ENZ resonance and pump wavelength at 1220 nm. An ultrafast redshift of the ENZ resonance is observed, indicating the increase in m^* induced by intraband transitions. A maximum of nonlinear response of $\Delta A = 100$ mOD is obtained at a pump fluence of $1000 \mu\text{J}/\text{cm}^2$, as shown in Fig. 9(a), corresponding to $\Delta T/T = 35\%$, which is comparable to values in the literature [8,20,28]. Additional ΔA spectral maps measured on ITO films with different ENZ wavelengths and pumped at their resonance peaks are plotted in Figs. 5(b) and Fig. 5(c). In Fig. 5(d) the spectrum immediately after the pump absorption (black curve) is fitted to determine m^* and E_g using the intraband transition model, followed by the Drude model and TMM analysis. In the fitting process, we assume two initial values for E_g and m^* . Since at room temperature 300 K the plasma frequency $\omega_{p,unpump}$ is known, the chemical potential $\mu(300 \text{ K})$ can be extracted from Eq. (4). Then $n(\mu, 300 \text{ K})$ and $U(\mu, 300 \text{ K})$ can be obtained. After the NIR pump, n remains unchanged for the intraband transition, which means $n = n(\mu, 300 \text{ K})$; therefore μ as a function of T is determined from Eq. (5). Equation (6) gives the electron temperature T with the specific dU , which represents the pump strength. Then $\omega_{p,pump}(\mu, T)$ can be calculated from Eq. (4). This intraband transition model helps determine E_g and m^* from the NIR pump transient spectra, where $\omega_{p,pump}$ is extracted by fitting the experimental data. The fitted spectrum [Fig. 5(d), red curve] is in good agreement with the experiment. Remaining deviations may be due to nonconstant E_g and ϵ_∞ in our theoretical model and experimental uncertainties. The same calculation is conducted on other samples with ENZ wavelengths at 1400 and 1500 nm [Figs. 5(e) and 5(f)]. The fitting values for all Drude and band-structure parameters are listed in Table II.

Next, a UV pulse centered at 360 nm (corresponding to the band gap of ITO films, Fig. 9(b) [43]) is used as a pump

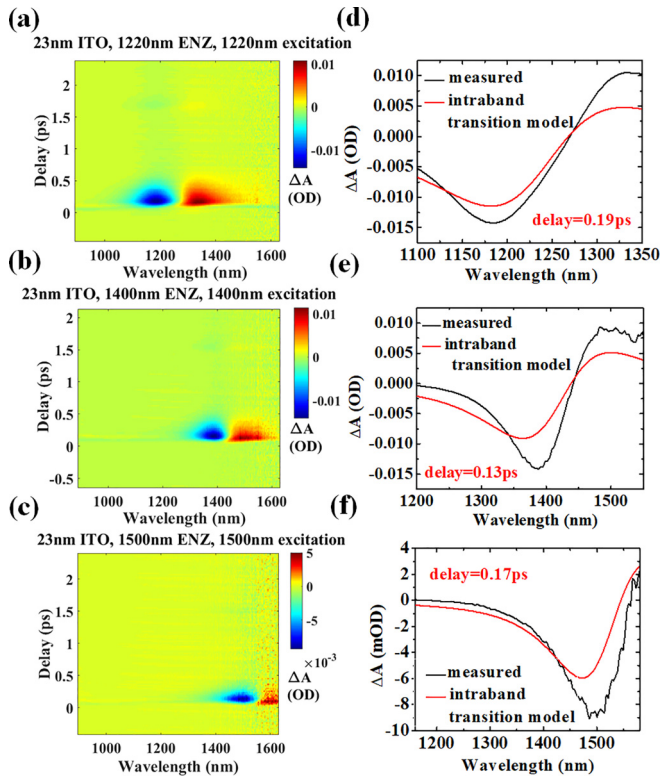


FIG. 5. (a)–(c) Time-resolved transmittance spectral change of ITO films. The pump wavelength coincides at the ENZ wavelength at (a) 1220 nm, (b) 1400 nm, and (c) 1500 nm. (d)–(f) ΔA spectra at the beginning of the relaxation process for ENZ wavelengths at (d) 1220 nm, (e) 1400 nm, and (f) 1500 nm. The black curves are extracted from the experimental data with the delay time at (d) 0.19 ps, (e) 0.13 ps, and (f) 0.17 ps. The red curves are theoretical spectra based on the intraband model. (f) Kinetic decay process of the absorbed energy dU .

TABLE I. Parameters used in sputtering ITO thin films.

λ_{ENZ} (nm)	Anneal temperature ($^{\circ}\text{C}$)	Anneal time (min)
1220	450	60
1400	600	60
1500	300	60

TABLE II. Drude and band structure parameters of ITO thin films.

λ_{ENZ} (nm)	ϵ_{∞} (eV)	ω_p (eV)	γ_p (eV)	m^* (m_0)	E_g (eV)
1220	3.75	1.95	0.2	0.13	1.77
1400	3.75	1.70	0.14	0.13	2.07
1500	3.75	1.58	0.11	0.43	2.64

pulse. The transient maps for the same films used in NIR experiments with varying ENZ wavelengths are shown in Figs. 6(a)–6(c). A different behavior is observed as a result of the competing mechanisms of interband and intraband absorption. The film with ENZ wavelength at 1220 nm has the largest nonparabolicity (Table II), and therefore the contribution of the intraband transition to ω_p is larger than the contribution of the interband transition. Thus, as shown in Fig. 6(a), the plasma frequency is redshifted, which is similar to the behavior exhibited under the NIR pump. In contrast to this, films with longer ENZ wavelengths have smaller nonparabolicity, which is not able to balance the shift induced by the free carrier density increase. Therefore ω_p is blueshifted [Figs. 6(b) and 6(c)], agreeing well with the theory shown in Fig. 4(c). Moreover, in Figs. 6(d)–6(f), the experimental spectra corresponding to the peak of ΔA are plotted along with the interband model calculation. Here the nonlinearity

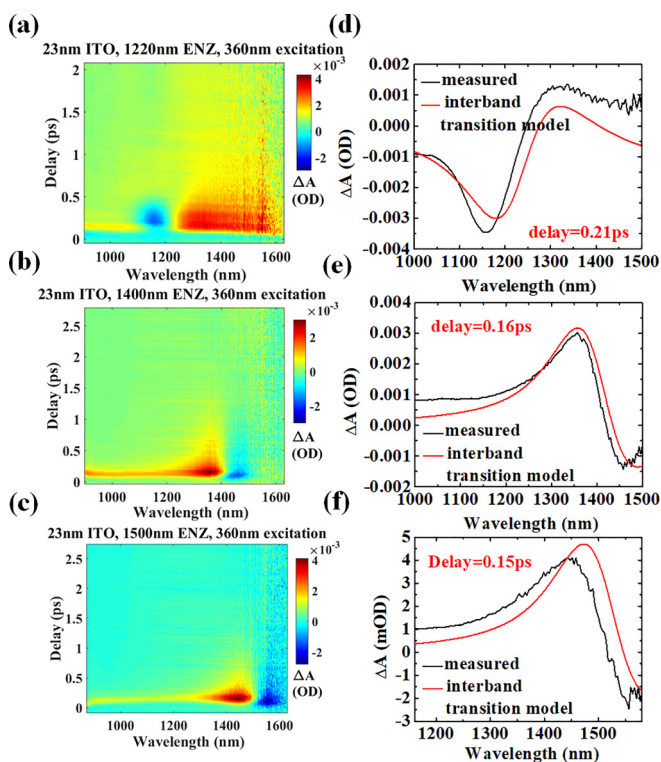


FIG. 6. (a)–(c) Time-resolved transmittance spectral change of ITO films at pump wavelength of 360 nm. The ENZ wavelength is at (a) 1220 nm, (b) 1400 nm, and (c) 1500 nm. (d)–(f) ΔA spectra at the beginning of the relaxation process for ENZ wavelengths at (d) 1220 nm, (e) 1400 nm, and (f) 1500 nm. The black curves are extracted from the experimental data with the delay time at (d) 0.21 ps, (e) 0.16 ps, and (f) 0.15 ps. The red curves are theoretically calculated using the interband transition model and the parameters in Table II.

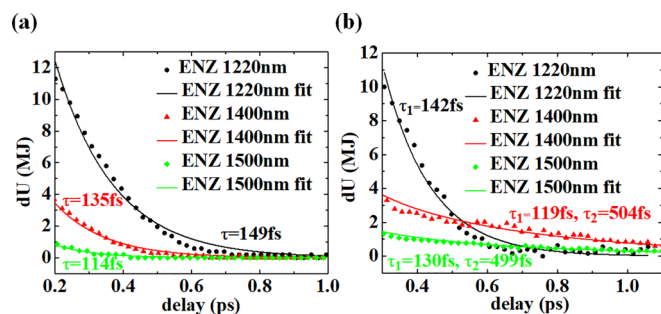


FIG. 7. Kinetic decay process of the absorbed energy dU under (a) NIR pump and (b) UV pump.

is calculated using all the necessary parameters ω_p , γ_p , E_g , and m^* that are determined under the NIR pump, as shown in Table II. By solving Eqs. (6) and (7) simultaneously, μ and T under the UV pump are determined, which can be plugged into Eq. (4) to calculate $\omega_{p,\text{pump}}$. It should be emphasized that the theoretical spectra under the UV pump require no fitting. Unlike the spectra in Figs. 5(d)–5(f), the red curves in Figs. 6(d)–6(f) are solely determined from the interband model and the parameters in Table II. These curves show a remarkable agreement with the experiments without any additional fitting procedure. Interestingly, these results seem to suggest that increased doping in ENZ materials tend to decrease the effective mass of electrons, which is the opposite effect compared to what one would expect from a quasiparticle interaction picture in Landau's Fermi liquid theory [44].

Finally, the ultrafast decay process is investigated. After the NIR excitation, the hot carriers cool down through the electron-phonon coupling on a sub-picosecond timescale [6,45]. The dissipation of the excitation energy density dU as a function of time is plotted in Fig. 7(a). Exponential fits estimate a relaxation time of ~ 100 fs, which agrees well with typical intraband transition dynamics [6]. While under UV excitation, the dynamics of the relaxation process involve thermal dissipation through electron-phonon interactions and recombination, including the radiative and the trap-assisted channels [46]. Generally, the recombination is slower than the thermal dissipation. As shown in Fig. 7(b) (black curve), the decay of dU in the film with the ENZ wavelength at 1220 nm shows a characteristic recovery time of 142 fs. This agrees with the typical thermal dissipation time revealed in Fig. 7(a), indicating the dominance of the intraband transition. In contrast, red and green curves in Fig. 7(b) are better fit with a bi-exponential model, which includes a slower decay with $\tau_2 \approx 500$ fs in addition to the faster decay τ_1 attributed to thermal dissipation. This longer relaxation rate may correspond to the recombination, which again indicates that interband transitions play a dominant role in ITO films with the ENZ at 1400 and 1500 nm. More discussion on time dynamics of the carrier concentration, Fermi-Dirac distribution, and the transient permittivity is presented in Appendix C and Fig. 8.

V. CONCLUSION

In conclusion, we report a comprehensive analytical and experimental study explaining the role of various mechanisms responsible for ultrafast nonlinear properties of ITO thin films

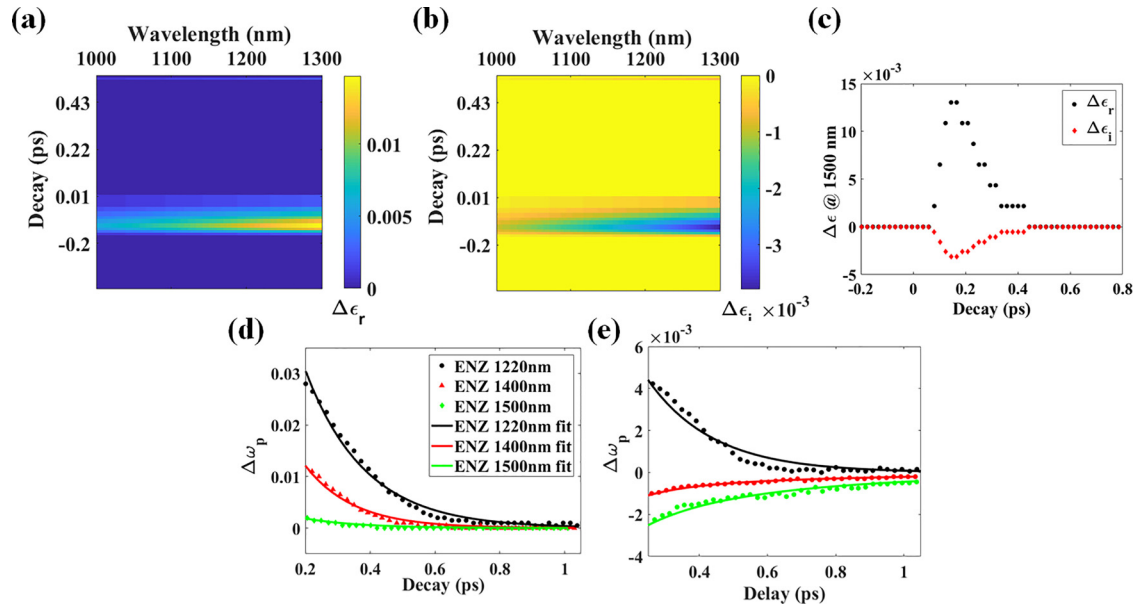


FIG. 8. (a) Transient spectral change of the real part of the permittivity $\Delta\epsilon_r$. (b) Transient spectral change of the imaginary part of the permittivity $\Delta\epsilon_i$. Both the ENZ wavelength and the pump wavelength are 1500 nm. (c) The time dynamics of $\Delta\epsilon_r$ and $\Delta\epsilon_i$ at 1500 nm. (d) The plasma frequency shift under NIR pump. (e) The plasma frequency shift under UV pump.

near their ENZ wavelengths. We have explored the interplay between the intraband transition, which increases the electron effective mass due to the nonparabolic band structure, and the interband transition, which generates larger free carrier concentrations. The combination of these processes under the above-band-gap pump results in different nonlinear behaviors predicting the cumulative shift direction of the plasma frequency and spectrally invertible nonlinearity. Moreover, the Drude and band structure parameters extracted from the fits show clear trends that are related to the material properties of ITO films. Therefore, ENZ materials are shown to be great optical platforms with tunable and invertible nonlinearities controlled solely by their intrinsic material properties. Our model will enable future exploration of nonlinear ENZ materials based on the competing mechanisms between nonparabolic band structure and the carrier density. The tailored nonlinearities can be used to guide the design and fabrication of TCO photonic platforms for desired optical functionalities.

ACKNOWLEDGMENTS

This work was supported by UDRI with Air Force Contract No. FA8651-20-D-0003. M.S.A., S.U.D., and J.W.A. are thankful for funding support through AFOSR Lab Tasks 22RWCOR002. H.H. acknowledges support from the Department of Energy (DE-SC0020101). The authors thank Luiz Santos for helpful discussions.

APPENDIX A: METHODS

The ITO thin films are deposited by rf magnetron sputtering on glass substrates at room temperature. The magnetron sputtering is performed in vacuum at pressure of 2×10^{-6} Torr, with an Ar gas flow of 12 sccm. It is followed by a postdeposition annealing process in nitrogen atmosphere to

redshift the ENZ wavelengths of ITO films to the NIR regime [40,47]. The annealing temperatures are shown in Table I. Additional tunability of the ENZ wavelength is achieved by cutting off the nitrogen gas flow during the annealing process, which increases the oxygen concentration in the atmosphere.

The oblique transmittance spectra are measured using a halogen lamp obliquely incident on the sample at various angles. The transmitted light is collected with a 10x objective (NA = 0.25). Transient transmittance experiments are performed by optically pumping the ITO thin films with a single-wavelength pulsed laser and probing the transmitted signals with a broadband white light continuum. The pump pulse is generated by using a Coherent Astrella Ti:sapphire amplified system centered at 800 nm and an optical parametric amplifier (OPA). The pulse length is approximately 35 fs, and the repetition frequency is 1 kHz. The broadband probe beam (800–1600 nm spectral range) is generated by focusing the output of the amplifier on a sapphire crystal. The probe beam is obliquely incident at 45 degrees, and the pump beam is deviated from it by a small angle. The probe beam is *p* polarized to support out-of-plane electric field components, and the pump beam is *s* polarized to avoid extra nonlinearity caused by two-beam coupling effects.

APPENDIX B: DRUDE AND BAND STRUCTURE PARAMETERS OF ITO THIN FILMS

Table II lists the values for all Drude and band structure parameters that are calculated using the intraband transition model. It shows that with the increase of the plasma frequency, the free carrier density will increase, giving rise to a higher Fermi level. This can be attributed to the sample annealing process where the grain size shrinks and more electrons are relaxed from the bound states. The

nonparabolicity generally also tends to increase with the plasma frequency. The reason could be the modification of the crystalline structure followed by the annealing process or doping-related band modification effects; however, more theoretical and experimental studies are needed to further understand this.

APPENDIX C: ADDITIONAL DISCUSSION ON TIME DYNAMICS

Additional discussion on the time dynamics of carrier concentration, Fermi-Dirac distribution, and transient permittivity is introduced in this section.

The carrier concentration of ITO films under the NIR pump does not change with time due to the sub-band-gap pump photon energy. The excitation energy dU is fully absorbed by the conduction band electrons, resulting in a hot electron distribution and raising the Fermi level. Thus the decay dynamics of the Fermi level is expected to follow the same trend as shown in Fig. 7(a). The time dynamics of the real and imaginary parts of the transient permittivity, $\Delta\epsilon_r$ and $\Delta\epsilon_i$, for ENZ wavelengths at 1500 nm, are shown in Figs. 8(a) and 8(b). Specifically, $\Delta\epsilon_r$ and $\Delta\epsilon_i$ at the probe wavelength of 1500 nm are shown in Fig. 8(c). To better illustrate the decay process, the transient shift of the plasma frequency, which can directly reflect the transient permittivity through the Drude model, is plotted in Fig. 8(d). The decay process shows the same characteristic lifetime as the decay of dU .

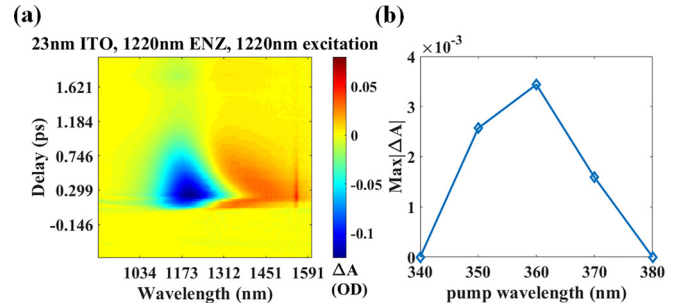


FIG. 9. (a) Time-resolved transmittance spectral change of the ITO thin film. The pump wavelength coincides with the ENZ wavelength at 1220 nm. The maximum $|\Delta A| = 126$ mOD under the $1000 \mu\text{J}/\text{cm}^2$ pump fluence corresponds to $\Delta T/T = 35\%$. (b) Pump-wavelength-dependent maximum $|\Delta A|$ in the UV region.

Second, both the carrier concentration and the Fermi level are raised under the UV pump, and therefore two characteristic recovery processes are expected, corresponding to the recombination and the electron-phonon interaction. As shown in Fig. 7(b), the carrier concentration decays through the recombination process with the lifetime τ_2 (red and green curves), and the Fermi level drops through both the electron-phonon interaction with a faster lifetime τ_1 and the recombination with a slower lifetime τ_2 . The transient shift of the plasma frequency is shown in Fig 8(e). Figure 9 shows the maximum observed change in the transmittance and its dependence on the pump photon energy.

- [1] N. Kinsey, C. DeVault, A. Boltasseva, and V. M. Shalaev, Near-zero-index materials for photonics, *Nat. Rev. Mater.* **4**, 742 (2019).
- [2] I. Liberal and N. Engheta, Near-zero refractive index photonics, *Nat. Photonics* **11**, 149 (2017).
- [3] Y. Li, S. Kita, P. Muñoz, O. Reshef, D. I. Vulis, M. Yin, M. Lončar, and E. Mazur, On-chip zero-index metamaterials, *Nat. Photonics* **9**, 738 (2015).
- [4] E. J. R. Vesceur, T. Coenen, H. Caglayan, N. Engheta, and A. Polman, Experimental Verification of $n=0$ Structures for Visible Light, *Phys. Rev. Lett.* **110**, 013902 (2013).
- [5] O. Reshef, P. Camayd-Muñoz, D. I. Vulis, Y. Li, M. Loncar, and E. Mazur, Direct observation of phase-free propagation in a silicon waveguide, *ACS Photonics* **4**, 2385 (2017).
- [6] M. Z. Alam, I. D. Leon, and R. W. Boyd, Large optical nonlinearity of indium tin oxide in its epsilon-near-zero region, *Science* **352**, 795 (2016).
- [7] M. H. Javani and M. I. Stockman, Real and Imaginary Properties of Epsilon-Near-Zero Materials, *Phys. Rev. Lett.* **117**, 107404 (2016).
- [8] M. Clerici, N. Kinsey, C. DeVault, J. Kim, E. G. Carnemolla, L. Caspani, A. Shaltout, D. Faccio, V. Shalaev, A. Boltasseva, and M. Ferrera, Controlling hybrid nonlinearities in transparent conducting oxides via two-colour excitation, *Nat. Commun.* **8**, 15829 (2017).
- [9] J. Kim, A. Dutta, G. V. Naik, A. J. Giles, F. J. Bezares, C. T. Ellis, J. G. Tischler, A. M. Mahmoud, H. Caglayan, O. J. Glembocki, A. V. Kildishev, J. D. Caldwell, A. Boltasseva, and N. Engheta, Role of epsilon-near-zero substrates in the optical response of plasmonic antennas, *Optica* **3**, 339 (2016).
- [10] Y. C. Jun, J. Reno, T. Ribaudou, E. Shaner, J. J. Greffet, S. Vassant, F. Marquier, M. Sinclair, and I. Brener, Epsilon-near-zero strong coupling in metamaterial-semiconductor hybrid structures, *Nano Lett.* **13**, 5391 (2013).
- [11] O. Reshef, I. De Leon, M. Z. Alam, and R. W. Boyd, Nonlinear optical effects in epsilon-near-zero media, *Nat. Rev. Mater.* **4**, 535 (2019).
- [12] N. Kinsey, C. DeVault, J. Kim, M. Ferrera, V. M. Shalaev, and A. Boltasseva, Epsilon-near-zero Al-doped ZnO for ultrafast switching at telecom wavelengths, *Optica* **2**, 616 (2015).
- [13] T. S. Luk, D. De Ceglia, S. Liu, G. A. Keeler, R. P. Prasankumar, M. A. Vincenti, M. Scalora, M. B. Sinclair, and S. Campione, Enhanced Third Harmonic Generation from the Epsilon-Near-Zero Modes of Ultrathin Films, *Appl. Phys. Lett.* **106**, 151103 (2015).
- [14] A. Capretti, Y. Wang, N. Engheta, and L. Dal Negro, Enhanced third-harmonic generation in Si-compatible epsilon-near-zero indium tin oxide nanolayers, *Opt. Lett.* **40**, 1500 (2015).
- [15] L. Caspani, R. P. M. Kaipurath, M. Clerici, M. Ferrera, T. Roger, J. Kim, N. Kinsey, M. Pietrzyk, A. Di Falco, V. M. Shalaev, A. Boltasseva, and D. Faccio, Enhanced Nonlinear Refractive Index in Epsilon-Near-Zero Materials, *Phys. Rev. Lett.* **116**, 233901 (2016).

- [16] S. Vezzoli, V. Bruno, C. DeVault, T. Roger, V. M. Shalaev, A. Boltasseva, M. Ferrera, M. Clerici, A. Dubietis, and D. Faccio, Optical Time Reversal from Time-Dependent Epsilon-Near-Zero Media, *Phys. Rev. Lett.* **120**, 043902 (2018).
- [17] M. S. Allen, J. W. Allen, B. R. Wenner, D. C. Look, and K. D. Leedy, Application of highly conductive ZnO to the excitation of long-range plasmons in symmetric hybrid waveguides, *Opt. Eng.* **52**, 064603 (2013).
- [18] S. Saha, B. T. Diroll, J. Shank, Z. Kudyshev, A. Dutta, S. N. Chowdhury, T. S. Luk, S. Campione, R. D. Schaller, V. M. Shalaev, A. Boltasseva, and M. G. Wood, Broadband, high-speed, and large-amplitude dynamic optical switching with yttrium-doped cadmium oxide, *Adv. Funct. Mater.* **30**, 1908377 (2020).
- [19] Y. Yang, K. Kelley, E. Sacht, S. Campione, T. S. Luk, J.-P. Maria, M. B. Sinclair, and I. Brener, Femtosecond optical polarization switching using a cadmium oxide-based perfect absorber, *Nat. Photonics* **11**, 390 (2017).
- [20] M. Z. Alam, S. A. Schulz, J. Upham, I. De Leon, and R. W. Boyd, Large optical nonlinearity of nanoantennas coupled to an epsilon-near-zero material, *Nat. Photonics* **12**, 79 (2018).
- [21] V. Bruno, C. DeVault, S. Vezzoli, Z. Kudyshev, T. Huq, S. Mignuzzi, A. Jacassi, S. Saha, Y. D. Shah, S. A. Maier, D. R. S. Cumming, A. Boltasseva, M. Ferrera, M. Clerici, D. Faccio, R. Sapienza, and V. M. Shalaev, Negative Refraction in Time-Varying Strongly Coupled Plasmonic-Antenna-Epsilon-Near-Zero Systems, *Phys. Rev. Lett.* **124**, 043902 (2020).
- [22] V. E. Babicheva, N. Kinsey, G. V. Naik, M. Ferrera, A. V. Lavrinenko, V. M. Shalaev, and A. Boltasseva, Towards CMOS-compatible nanophotonics: Ultra-compact modulators using alternative plasmonic materials, *Opt. Express* **21**, 27326 (2013).
- [23] V. E. Babicheva, A. Boltasseva, and A. V. Lavrinenko, Transparent conducting oxides for electro-optical plasmonic modulators, *Nanophotonics* **4**, 165 (2015).
- [24] I. Liberal and N. Engheta, The rise of near-zero-index technologies, *Science* **358**, 1540 (2017).
- [25] P. Johnson and R. Christy, Optical constants of transition metals: Ti, V, Cr, Mn, Fe, Co, Ni, and Pd, *Phys. Rev. B* **9**, 5056 (1974).
- [26] T. Tyborski, S. Kalusniak, S. Sadofev, F. Henneberger, M. Woerner, and T. Elsaesser, Ultrafast Nonlinear Response of Bulk Plasmons in Highly Doped ZnO Layers, *Phys. Rev. Lett.* **115**, 147401 (2015).
- [27] P. Guo, R. D. Schaller, L. E. Ocola, B. T. Diroll, J. B. Ketterson, and R. P. Chang, Large optical nonlinearity of ITO nanorods for sub-picosecond all-optical modulation of the full-visible spectrum, *Nat. Commun.* **7**, 12892 (2016).
- [28] P. Guo, R. D. Schaller, J. B. Ketterson, and R. P. H. Chang, Ultrafast switching of tunable infrared plasmons in indium tin oxide nanorod arrays with large absolute amplitude, *Nat. Photonics* **10**, 267 (2016).
- [29] J. R. Hendrickson, S. Vangala, C. Dass, R. Gibson, J. Goldsmith, K. Leedy, D. E. Walker, J. W. Cleary, W. Kim, and J. Guo, Coupling of epsilon-near-zero mode to gap plasmon mode for flat-top wideband perfect light absorption, *ACS Photonics* **5**, 776 (2018).
- [30] C. K. Dass, H. Kwon, S. Vangala, E. M. Smith, J. W. Cleary, J. Guo, A. Alù, and J. R. Hendrickson, Gap-plasmon-enhanced second-harmonic generation in epsilon-near-zero nanolayers, *ACS Photonics* **7**, 174 (2020).
- [31] S. Campione, J. R. Wendt, G. A. Keeler, and T. S. Luk, Near-infrared strong coupling between metamaterials and epsilon-near-zero modes in degenerately doped semiconductor nanolayers, *ACS Photonics* **3**, 293 (2016).
- [32] B. C. Yildiz and H. Caglayan, Epsilon-near-zero media coupled with localized surface plasmon modes, *Phys. Rev. B* **102**, 165303 (2020).
- [33] E. Feigenbaum, K. Diest, and H. A. Atwater, Unity-order index change in transparent conducting oxides at visible frequencies, *Nano Lett.* **10**, 2111 (2010).
- [34] Y. Zhou, M. Z. Alam, M. Karimi, J. Upham, O. Reshef, C. Liu, A. E. Willner, and R. W. Boyd, Broadband frequency translation through time refraction in an epsilon-near-zero material, *Nat. Commun.* **11**, 2180 (2020).
- [35] R. Secondo, A. Ball, B. Diroll, D. Fomra, K. Ding, V. Avrutin, Ü. Özgür, D. Demchenko, J. Khurgin, and N. Kinsey, Deterministic modeling of hybrid nonlinear effects in epsilon-near-zero thin films, *Appl. Phys. Lett.* **120**, 031103 (2022).
- [36] J. Bohn, T. S. Luk, C. Tollerton, S. W. Hutchings, I. Brener, S. Horsley, W. L. Barnes, and E. Hendry, All-optical switching of an epsilon-near-zero plasmon resonance in indium tin oxide, *Nat. Commun.* **12**, 1017 (2021).
- [37] R. Secondo, J. Khurgin, and N. Kinsey, Absorptive loss and band non-parabolicity as a physical origin of large nonlinearity in epsilon-near-zero materials, *Opt. Mater. Express* **10**, 1545 (2020).
- [38] X. Liu, J. Park, J.-H. Kang, H. Yuan, Y. Cui, H. Y. Hwang, and M. L. Brongersma, Quantification and impact of nonparabolicity of the conduction band of indium tin oxide on its plasmonic properties, *Appl. Phys. Lett.* **105**, 181117 (2014).
- [39] M. Born and E. Wolf, *Principles of Optics: Electromagnetic Theory of Propagation, Interference and Diffraction of Light* (Elsevier, New York, 2013).
- [40] Y. Wang, A. Capretti, and L. Dal Negro, Wide tuning of the optical and structural properties of alternative plasmonic materials, *Opt. Mater. Express* **5**, 2415 (2015).
- [41] E. O. Kane, Band structure of indium antimonide, *J. Phys. Chem. Solids* **1**, 249 (1957).
- [42] M. H. Cohen, Energy bands in the bismuth structure. I. A nonellipsoidal model for electrons in Bi, *Phys. Rev.* **121**, 387 (1961).
- [43] Z. Yu, I. R. Perera, T. Daeneke, S. Makuta, Y. Tachibana, J. J. Jasieniak, A. Mishra, P. Bäuerle, L. Spiccia, and U. Bach, Indium tin oxide as a semiconductor material in efficient p-type dye-sensitized solar cells, *NPG Asia Mater.* **8**, e305 (2016).
- [44] S. Azadi, N. D. Drummond, and W. M. C. Foulkes, Quasiparticle Effective Mass of the Three-Dimensional Fermi Liquid by Quantum Monte Carlo, *Phys. Rev. Lett.* **127**, 086401 (2021).
- [45] N. Del Fatti, C. Voisin, M. Achermann, S. Tzortzakis, D. Christofilos, and F. Vallée, Nonequilibrium electron dynamics in noble metals, *Phys. Rev. B* **61**, 16956 (2000).
- [46] S. M. Sze, Y. Li, and K. K. Ng, *Physics of Semiconductor Devices* (John Wiley & Sons, New York, 2021).
- [47] Y. Wang, A. C. Overvig, S. Shrestha, R. Zhang, R. Wang, N. Yu, and L. Dal Negro, Tunability of indium tin oxide materials for mid-infrared plasmonics applications, *Opt. Mater. Express* **7**, 2727 (2017).